Geophysical Research Letters

RESEARCH LETTER
10.1029/2019GL082201

Distribution of Crustal Melt Bodies at the Hot Spot-Influenced Section of the Galápagos Spreading Centre From Seismic Reflection Images

B. Boddupalli[1] and J.P. Canales[2]

[1]National Oceanography Centre Southampton, University of Southampton, Southampton, UK, [2]Department of Geology and Geophysics, Woods Hole Oceanographic Institution, Woods Hole, MA, USA

Key Points:
- Seismic images from the hot spot-influenced section of the Galápagos spreading center reveal a multisill magmatic system in the lower crust
- Spatial correlation between a gap in the axial melt lens and the location of a mature, waning seafloor hydrothermal field suggests magmatic-hydrothermal interactions
- Evidence for off-axis melt lenses emplaced at the edges of the axial low velocity zone, and weak Moho reflections on the across ridge axis seismic profile, which disappear in the axial zone

Supporting Information:
- Supporting Information S1

Correspondence to:
B. Boddupalli,
b.boddupalli@soton.ac.uk

Citation:
Boddupalli, B., & Canales, J. P. (2019). Distribution of crustal melt bodies at the hot spot-influenced section of the Galápagos Spreading Centre from seismic reflection images. *Geophysical Research Letters*, *46*, 4664–4673. https://doi.org/10.1029/2019GL082201

Received 25 JAN 2019
Accepted 22 APR 2019
Accepted article online 29 APR 2019
Published online 13 MAY 2019

Abstract Accretion of the lower crust at mid-ocean ridges is a debated topic, with modern seismic observations pointing to a complex magmatic system that includes an axial multisill system of middle- and lower-crustal melt lenses and near- and off-axis melt bodies. Here we revisit the hot spot-influenced section of the western Galápagos Spreading Centre and reprocess multichannel seismic reflection data using a wide-angle seismic tomography model. Our new images show that the magma reservoir in the lower crust at this ridge section is intruded with partially molten melt lenses. The images also show evidence for off-axis melt lenses, magmatic-hydrothermal interactions and Moho reflections in this region. We conclude that the similarities between the axial crustal structure of this hot spot-influenced mid-ocean ridge and the multisill magmatic structure imaged at the East Pacific Rise indicate that these features are common along the global mid-ocean ridge system where seafloor spreading is dominated by magmatic accretion.

Plain Language Summary New oceanic crust forms along mid-ocean ridges from melt extracted from the upwelling mantle. Accretion of the upper crust is well understood, but the process involved in the accretion of the lower crust is still debated. Here we present new seismic images of the crustal magmatic system of the western Galápagos Spreading Centre in the region where the influence of the Galápagos hot spot is largest and ridge magmatism is most robust. Our images show a complex magmatic system that includes lenses of partially molten rock beneath the spreading axis from the midcrust at 1.5 km and throughout the lower crust down to at least 5.4 km below the seafloor and off-axis melt bodies. Segmentation of the axial magmatic system correlates with presence of hydrothermal features on the seafloor. This system has characteristics very similar to those recently imaged at the East Pacific Rise, indicating that these features are representative of crustal accretion at mid-ocean ridges where seafloor spreading is dominated by magmatic processes.

1. Introduction

Seismic reflection imaging has been instrumental for the study of the physical structure of magmatic systems beneath intermediate to (ultra)fast-spreading mid-ocean ridges (MORs) where seafloor spreading is magmatically dominated (e.g., Detrick et al., 1987). Studies from the late 1980s through the 2000s showed that the upper oceanic crust is constructed from dyking and seafloor eruptions from magma that accumulates predominantly within a thin axial melt lens (AML) at ~1–3 km below seafloor (bsf; e.g., Kent et al., 1993). The AML marks the top of a broad region characterized by low seismic velocities and high attenuation indicative of elevated temperatures and partial melt (e.g., Dunn et al., 2000; Wilcock et al., 1995). However, the absence in those early studies of other crustal reflectors in the axial region, aside from the AML, contributed to the debate of possible models about melt transport from the mantle to the AML and the accretion of the lower crust (e.g., Maclennan et al., 2004). The possible models range from the lower crust crystallizing from the shallow AML (i.e., gabbro glacier model; Henstock et al., 1993; Quick & Denlinger, 1993) to a dual-sill or multisill models (Boudier et al., 1996; Kelemen et al., 1997). Our understanding about crustal accretion has been changing during the last decade as improved seismic reflection images from different settings provided evidence for more complex crustal magmatic systems. Recent evidence include segmentation of the AML (Carbotte et al., 2013; Marjanović et al., 2018), crustal axial melt sills below the

AML (Arnulf et al., 2014; Marjanović et al., 2018), lower crustal sills in the near axis region (Canales et al., 2009), and off-axis magmatic systems (Aghaei et al., 2017; Canales et al., 2012; Han et al., 2014).

The relationship between the recent seismic observations of crustal sills and the axial low velocity zone (LVZ) imaged by seismic tomography is unclear due to the paucity of colocated wide-angle seismic velocity models and modern multichannel seismic (MCS) images. The three-dimensional (3-D) MCS study of the East Pacific Rise (EPR) at 9°38–57′N (Mutter et al., 2009) indicates that off-axis melt lenses (OAMLs) form close to but outside of the axial LVZ (Canales et al., 2012; Han et al., 2014), based on two-dimensional (2-D) and 3-D wide-angle tomography models from nearby regions (Canales et al., 2012; Dunn et al., 2000). However other features such as subaxial melt lenses (SAMLs; Marjanović et al., 2014) lack background *P* wave velocity models that would add context and additional constraints to their interpretation.

In this work, we revisit the hot spot-influenced section of the western Galápagos Spreading Centre (GSC) where coincident 2-D MCS data (Blacic et al., 2004) and 3-D crustal tomography models are available (Canales et al., 2014). Previous studies using the MCS data set focused on poststack time-migrated imaging of the Moho ~20–30 km to the north of the ridge axis (Canales et al., 2002) and shallow axial and near-axis structure (layer 2A thickness and depth to the AMLs; Blacic et al., 2004). However, middle and lower crustal structure in the near-axis region was not addressed in those studies. Here we use a prestack depth migration (PSDM) approach to reprocess the MCS data with the assistance of the tomography-derived *P* wave velocity model (Canales et al., 2014). Our new images reveal new features that were not observed in the existing poststack time-migrated images, which we interpret as OAMLs and SAMLs, in addition to the previously recognized AML and Moho reflectors. We then conduct a joint interpretation of the new observations and the existing 3-D *P* wave velocity model that allows us to explore the spatial relationships between the tomography-inferred magma reservoirs and the MCS-imaged melt lenses.

2. Tectonic Setting

The GSC forms a divergent plate boundary separating the Cocos plate from the Nazca plate, currently spreading at intermediate rates increasing eastward from 53 mm/year at 97°W to 58 mm/year at 91°W (full rates; Wilson & Hey, 1995). Seafloor spreading in this region initiated 25 Myr ago with the breakup of the Farallon plate along a fracture zone near the Galápagos hot spot (Hey & Vogt, 1977). The Galápagos hot spot is located ~200 km south of the GSC near 92°W on the western edge of the Galápagos Archipelago. The Galápagos transform fault located near 90°50′W divides the GSC into two sections: western and eastern (e.g., Christie et al., 2005; Sinton et al., 2003).

Along the western GSC, the influence of the hot spot is most pronounced between 93.25°W and the 90°50′W transform fault, where the ridge forms a 20- to 30-km-wide, 400- to 700-m-high axial high with mantle Bouguer anomaly and crustal thickness reaching their minimum and maximum, respectively, along the axis (Canales et al., 2002; Detrick et al., 2002; Ito & Lin, 1995). In this region, complex volcanic lineaments extending between the Galápagos Islands and the GSC are inferred to be a result of the interplay between plume-ridge interactions and lithospheric stresses (Harpp & Geist, 2002; Mittelstaedt et al., 2012). Multibeam bathymetric studies have revealed the fine-scale axial segmentation (<2 km), with right-stepping offsets on the spreading axis attributed to the southward displacement of the axis where volcanic lineaments intersect the ridge (Sinton et al., 2003). An extensive near-bottom hydrographical survey along the GSC between 91°10′W and 94°30′N found evidence for surprisingly scarce high-temperature hydrothermal venting (Baker et al., 2008), with only two confirmed active black smoker fields in the hot spot influence section of the western GSC near 92°W (Figure 1) and one near 94°W (Haymon et al., 2008).

East of 92.5°W, crustal thickness is 7.5 km (Canales et al., 2002; Canales et al., 2014), and the depth of the ~0.5- to 1.5-km-wide AML as observed in the multichannel seismic reflection imaging is 1.0–2.5 km bsf (Blacic et al., 2004). The variation in the thickness of the layer 2A as observed on the time-migrated seismic sections nearly increases by 150% away from the axis where it is 0.24–0.42 km thick (Blacic et al., 2004). Results from wide-angle seismic tomography predict melt throughout the lower crust with a lower crustal reservoir at 3–4 km bsf containing up to ~2–7% melt (dependent on melt topology; Canales et al., 2014). The alignment of these reservoirs with depth is not vertical but rather shows a gradual shift toward the south flank of the ridge axis (Canales et al., 2014). It is proposed that the Moho reservoir feeds the lower-crustal reservoir, which in turn feeds magma to the midcrustal melt lens (Canales et al., 2014). The high magma

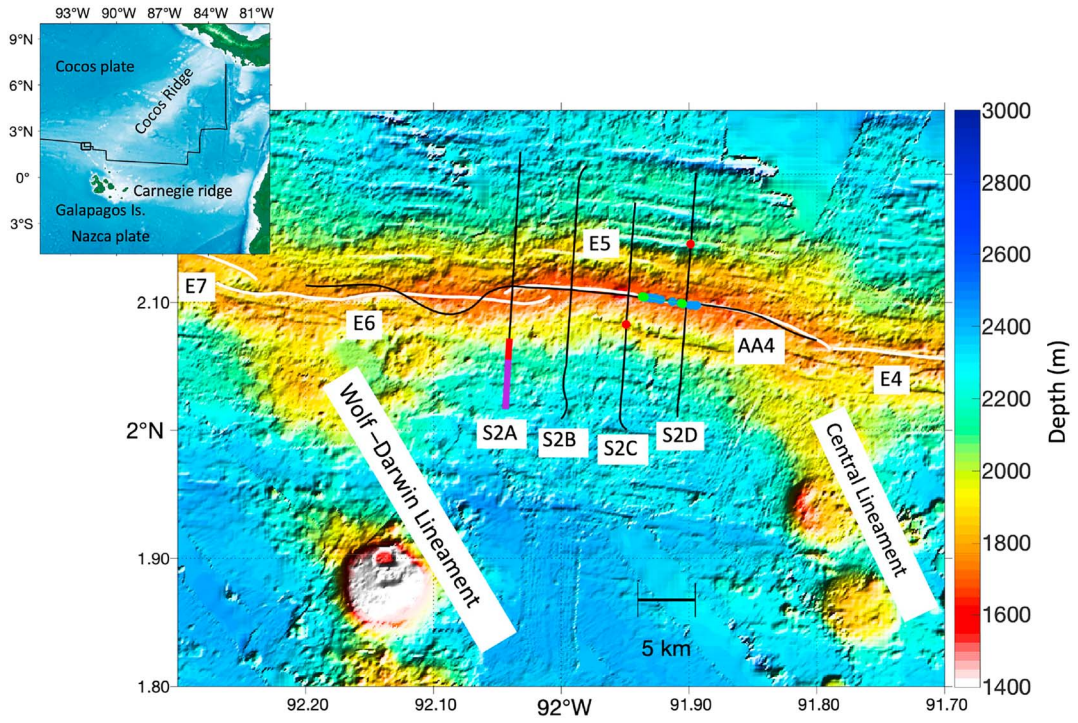

Figure 1. Bathymetry map of the Eastern Province of the western GSC (following the nomenclature of Sinton et al., 2003) near the Wolf-Darwin and Central volcanic lineaments (Mittelstaedt et al., 2012). Ridge axis as defined by Sinton et al. (2003) is shown with a white solid line, and EW0004 seismic profiles AA4, S2A, S2B, S2C, and S2D used in this study are shown in black bold curves. The location of the off-axis melt lenses and the Moho reflections on profiles S2A, S2C, and S2D shown in Figures 2 and 3 are highlighted by red and dark violet, respectively. Between the profiles S2C and S2D, we highlight active and inactive black smoker fields in green and blue dots, respectively, along the AA4 profile. The two highlighted active black smoker fields going west to east are the Iguanas and the Pinguinos. Inset shows location of the study area in the eastern Equatorial Pacific.

supply in the proximity of the hot spot favors the formation of the midcrustal reservoir and also imparts greater chemical signature variations to the magma (Rubin & Sinton, 2007).

3. Data and Processing

Multichannel and wide-angle seismic data sets at the GSC were acquired as part of cruise EW00-04 during April–May 2000, on R/V Maurice Ewing (Detrick & Sinton, 2014). In the reflection survey, ~86% of the length of the ridge axis between ~95.5°W and 91.25°W was surveyed, with nearly 100% coverage east of 94.5°W. Fifteen cross-axis profiles were also acquired, which extended at least 10 km north and south of the ridge. In this study, we have reprocessed five of the EW00-04 seismic profiles located near 92°W between the Central and Wolf-Darwin (WDL) volcanic lineaments: one along the ridge axis and four perpendicular to the ridge axis (Figure 1). The air gun system was comprised of two arrays of 10 air guns (total volume of 0.143 cubic metres) towed at a depth of ~8 m. Shooting interval was 15 s with a 50-ms randomization window to minimize noise from previous shots. The shot interval and ship speed of 4.5 kts yielded ~38-m shot spacing. A 6-km-long, 480-channel streamer was used to record 10 s of data at a sampling interval of 4 ms. The 480 channels of the streamer with spacing of 12.5 m resulted in 80-fold common-midpoint (CMP) gathers.

The prestack processing sequence is consisted of the following (supporting information Figure S3A): (1) CMP geometry definition for all seismic data traces; (2) band-pass filtering (1-6-100-125 Hz); (3) noise attenuation using the LIFT method, a processing technique that suppresses noise while reconstructing signal to its original form preserving amplitude integrity (Aghaei et al., 2014; Choo et al., 2004; Han et al., 2016; Figure S3B); (4) offset-dependent spherical divergence correction to compensate for geometrical spreading; (5) surface-consistent amplitude balancing to normalize abnormally high/low shot and channel amplitudes; and (6) seafloor primary multiple mute to reduce migration noise.

Following the processing, we applied a PSDM algorithm based on decomposition of the wavefield into plane waves and depth imaging using a wave equation, finite-difference frequency-distance prestack migration of each plane wave (Soubaras, 1996). The 2-D velocity models used for PSDM were extracted from a 3-D velocity model derived from ocean bottom hydrophone (OBH) wide-angle tomography (Canales et al., 2014). For migration of the along-axis profile, a 1-D velocity profile was extracted from the location of intersection of the north-south oriented OBH line with the ridge axis due to limited coverage of the rays along the ridge axis in the OBH survey. This profile was attached to the bottom of the water column velocity profile along the profile AA4 and extrapolated to 15-km depth. For migration of the cross-axis profiles, a 2-D velocity profile was extracted from the 3-D tomography model along the cross-axis OBH line and extrapolated to 15-km depth (Figure S1). Then the 2-D model was adjusted to the bathymetry data along each individual cross-axis profile. Postmigration steps included frequency-wavenumber (FK) enhancement of flat events, lateral mean filter, and depth-dependent gain.

4. Results and Discussion

Compared to the previous poststack time-migrated images of Blacic et al. (2004), our new PSDM images show a similar AML distribution but significant improvement in the imaging of features below the AML and in the near-axis region (Figures 2 and 3). One important difference is that our PSDM images do not image the base of layer 2A, which was well resolved in the Blacic et al. (2004) sections. The reasons for this observation are that the velocity model is poorly constrained at shallow depths and that the base of layer 2A is in most cases a high-gradient zone instead of a true reflector that is best imaged by stacking the far-offset retrograde branch of the 2A refraction (Harding et al., 1993). To aid our interpretation, we show our 2-D PSDM sections together with bathymetry and location of the ridge and with *P* wave velocity variations (relative to a 1-D structure, Figure S2) extracted from the 3-D velocity volume to highlight the correlation between LVZs and the identified features. We identify several interesting features in our images: AML, OAMLs, SAMLs, and the Moho.

4.1. AML

The AML in our images is a discontinuous feature along the axis of segment E5 at depths of 1.4–2 km bsf. This apparent variability was previously reported by Blacic et al. (2004), and it likely represents true geological small-scale segmentation of the AML, as observed in other similar setting (Carbotte et al., 2016). Although the AML spatial variability could also be an artifact due to data acquisition problems such as streamer feathering or deviations of the profile from the axis, we find this possibility unlikely because maximum deviation of profile AA4 from the morphological axis occurs between profiles S2B and S2C (Figure 1), where the AML is well imaged (Figure 2A).

None of our cross-axis profiles cross the ridge in locations where the AML is most prominently imaged on AA4. The intersection of profiles S2A and AA4 occurs at an overlapping spreading center with offset <2 km (Figure 2), which is a result of the southward displacement of segment E6 due to the influence of the WDL (Sinton et al., 2003). The AML on S2A is identified below the southern limb of the overlapping spreading center at depth of 2.2–2.4 km bsf (Figure 2B). Profiles S2B, S2C, and S2D are located near the edges of the AML segments (Figure 2A), although we see clear AML reflection sitting at the top of the LVZ at a depth of 1.5 km bsf at the intersection of profiles S2D and AA4 (Figure 3A).

A striking feature is the ~4-km-long gap in AML found at the center of segment E5, roughly between the locations of profiles S2C and S2D (Figure 2A). Interestingly, this AML gap coincides spatially with the Iguanas-Pinguinos Hydrothermal Field (IPHF; Haymon et al., 2008; Figures 2A and 3B). This mature and waning field is characterized by clusters of high-temperature active black smoker chimneys that are located over the edges of the AML gap (Figure 3B): the Iguanas black smokers over the transition between the AML gap and the AML reflector to the west of profile S2C, and the Pinguinos black smokers over the transition between the AML gap and the AML reflector to the east of profile S2D. The IPHF includes scores of recently inactive chimneys and vent biological communities distributed between the active sites over the AML gap (Figure 3B). Aside from prominent plume anomalies over the IPHF, the hydrographic surveys in this region did not detect significant plume activity anywhere else along segment E5 except weak plume signals further east to 91.8°W (Baker et al., 2008) over the prominent AML section east of profile S2D (Figure 3B). Based on these observations, we suggest that the current characteristics of the IPHF and the underlying AML

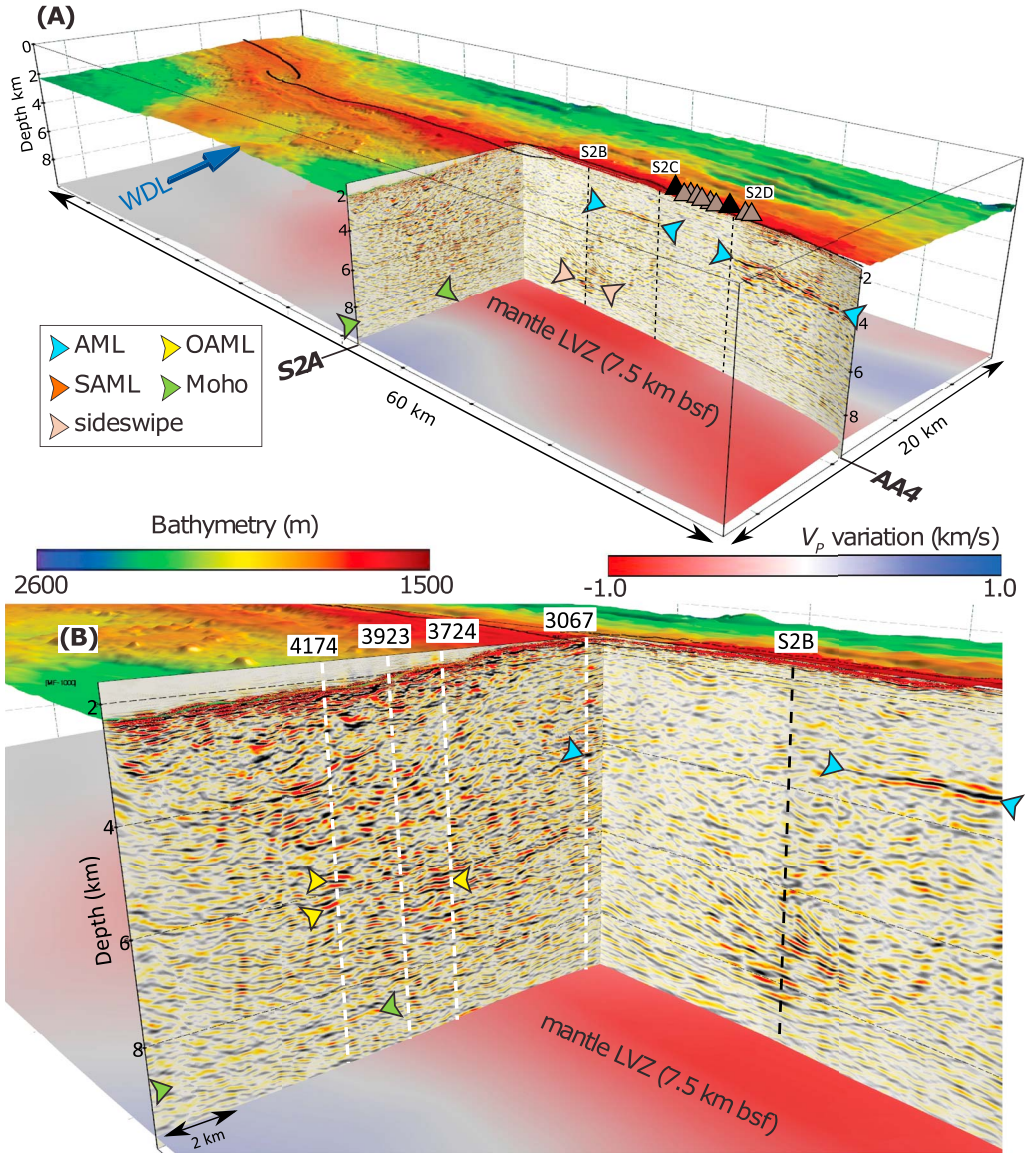

Figure 2. (A) Three-dimensional perspective of bathymetry, *P* wave velocity structure at a depth of 7.5 km below seafloor (bsf) and migrated sections for profiles AA4 and S2A. Colored arrowheads point to the most prominent crustal events interpreted in this study: axial melt lens (AML), subaxial melt lens (SAML), off-axis melt lens (OAML), and the Moho. Note Moho reflections are observed away from the mantle low velocity zone (LVZ) but are absent above it within ~3 km of the ridge axis. The dashed vertical lines are the intersection of the profiles S2B, S2C, and S2D with profile AA4. Ridge axis is shown with solid lines, and the blue arrow indicates the Wolf-Darwin lineament (WDL). The active and inactive black smoker fields are marked as black and gray triangles, respectively, along the profile AA4. (B). Zoomed-in view of profiles S2A and AA4, with *P* wave velocity variation shown at 7.5 km bsf. OAMLs tend to be located at or near the edge of the crustal LVZ, ~3–5 km off axis. *P* wave velocity structure is shown as variation relative to a 1-D reference model from the 3-D tomography model of Canales et al. (2014). Labeled dashed vertical white lines locate the CMP supergathers shown in Figures S4 and S5.

segmentation are linked to each other. If AML segmentation is controlled by melt delivery from the mantle and lower crustal melt focusing (Carbotte et al., 2013), then the AML gap represent a decrease in melt delivery from the mantle or the lower crust to the AML at lateral scales of a few kilometers. The decrease of melt influx to the AML and its eventual solidification would then have resulted in waning of hydrothermal activity at the IPHF (i.e., a bottom-up model of magmatic-hydrothermal interactions), as evidenced by the inactive chimneys. At present, high-temperature circulation is restricted to the edges of the AML gap where fluids can tap heat form the neighboring, more melt-rich AML segments.

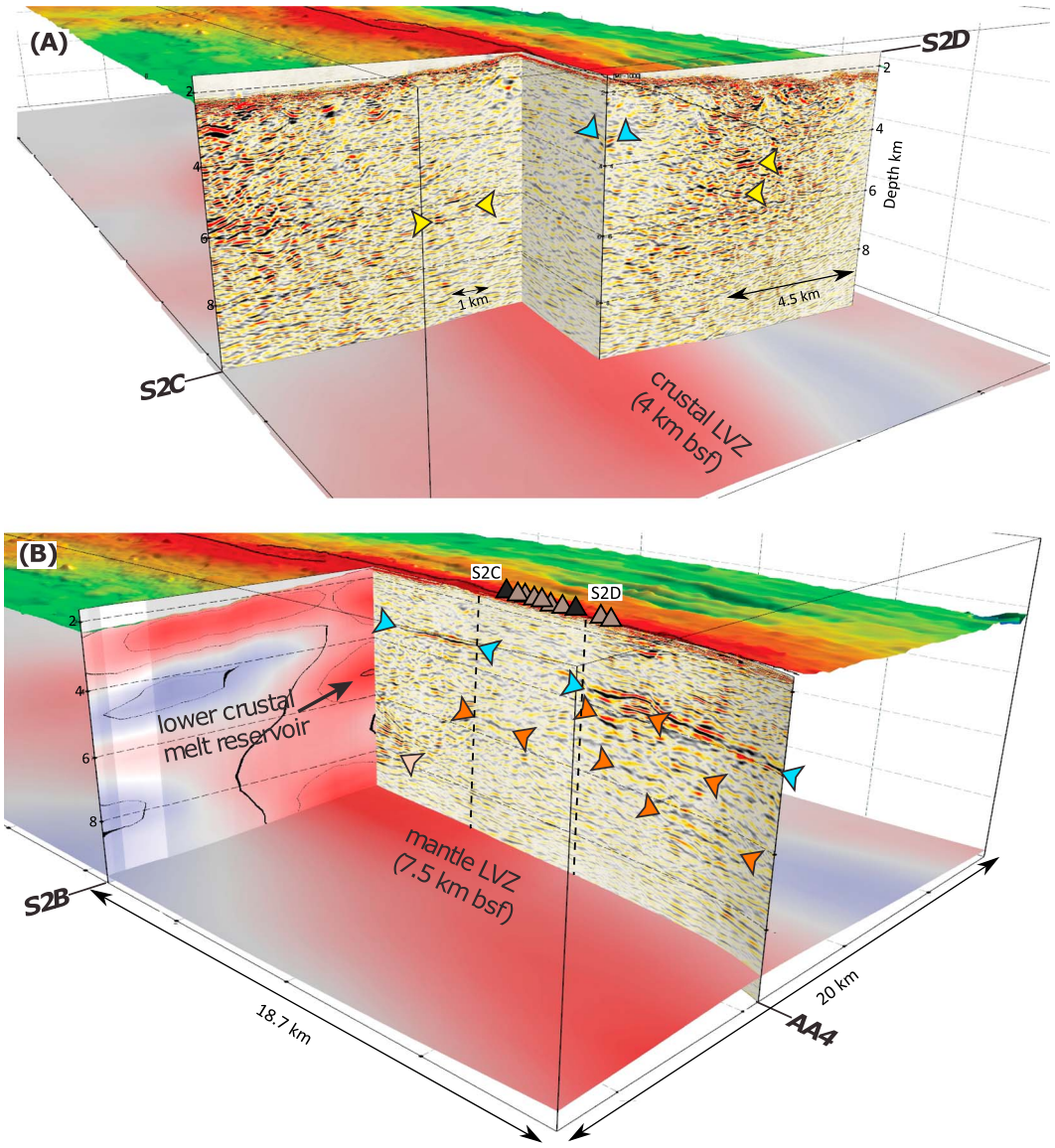

Figure 3. (A) Three-dimensional perspective of bathymetry; migrated sections for profiles AA4, S2C, and S2D; and *P* wave velocity structure at the depth of 4 km below the seafloor. Note that the velocity slice is shifted down by 4 km in depth for the sake of visual clarity. Off-axis melt lenses tend to be located at or near the edge of the crustal low velocity zone (LVZ), ~4–5 km off axis. (B) Three-dimensional perspective of bathymetry, *P* wave velocity structure at a depth of 7.5 km below seafloor (bsf) and along profile S2B, and migrated sections for profile AA4. Subaxial melt lenses are located up to ~2.5 km below the axial melt lens within a lower crustal melt reservoir (Canales et al., 2014). *P* wave velocity perturbation along S2B is shown with contours every 0.25 km/s (except the 0-km/s contour) to emphasize the lower crustal melt reservoir. Legend for colored arrowheads and other features as in Figure 2. The active and inactive black smoker fields are marked as black and gray triangles, respectively, along the profile AA4.

Alternatively, numerical models indicate that AML segmentation can be influenced by hydrothermal circulation cooling and solidifying the AML (Fontaine et al., 2011). In this case, favorable upper crustal permeability conditions could have led to localization of vigorous hydrothermal activity in the IPHF, as evidenced by the scarce hydrothermal plume activity in the other regions of segment E5. In this top-down model of magmatic-hydrothermal interactions, hydrothermal convection eventually leads to solidification of the AML and formation of the gap under the IPHF. As in the bottom-up scenario, solidification of the AML would lead to waning of hydrothermal activity and focusing of black smoker activity at the edges of the AML gap.

4.2. SAMLs

On the along-axis seismic section AA4, we observe horizontal, discontinuous reflections below the AML, which we interpret as lower-crustal magma sills (Figure 3), similar to those observed at the EPR (Marjanović et al., 2014). Assuming the dominant data signal frequency of our data is ~10–25 Hz and the background *P* wave velocity is 6.5 km/s (Canales et al., 2014), the strongest responses will be from the melt lenses of thickness between ~65 and 160 m as a single reflector. Lenses with thickness greater than 160 m will be characterized by a pair of opposite polarities from the top and the bottom interface of the lens, which we do not observe in our images.

The identified sills are more prevalent within the depth range where the tomography-derived crustal LVZ is most prominent. Although the 3-D traveltime tomography velocity model does not resolve small-scale structures of the size of a single sill (Canales et al., 2014), the migrated MCS data show that sills form within this crustal section interpreted as a lower-crustal reservoir containing up to 7% melt (Canales et al., 2014). These authors proposed that the formation of the intermediate crustal reservoir is favored by a thicker crust due to increased magma supply under the influence of the hot spot. With an increased crustal thickness, the melt extracted from the sub-Moho reservoir travels longer distances toward the AML, thus providing more opportunities for developing permeability barriers within crystallizing gabbros (Kelemen & Aharonov, 1998).

The observation of SAMLs in the region between profiles S2C and S2D where the AML is absent (Figure 3B) suggests that transfer of melt from the lower crustal reservoir to the shallow crustal reservoir is episodic and requires a melt fraction threshold in the SAML to be exceeded before melt if transferred from the SAML to the overlying AML, probably via hydrofracturing (Korenaga & Kelemen, 1998). Alternatively, if the AML receives melts from the SAML via continuous porous flow (e.g., Lissenberg et al., 2013), then melt solidification in the AML by hydrothermal cooling in this region has to be more efficient than AML replenishment from below.

4.3. OAMLs

Along the cross-axis profiles we have identified events located ~4–6 km away from the axial center and at depths between 3 and 5 km bsf (Figures 2 and 3) that we interpret as OAMLs. This interpretation is based in part on the character of these events as observed in unmigrated super CMP gathers, which is similar to the character of the AML event (Figures S4 and S5). In the cross-axis direction, the AML is observed as a near-offset reflection at 0.94 s two-way travel time (twtt) bsf (Figure S4A), and the OAMLs are observed also as near-offset reflections at ~1.1–1.6 s bsf (Figures S4B and S4C). Most importantly, some of the OAML events have the same waveform polarity as the AML, which is reversed relative to the seafloor reflection polarity (Figure S5). A reversed polarity is indicative of a velocity inversion, and it has been traditionally used as evidence for the partially molten character of AMLs at MORs (Canales et al., 2012; Collier & Sinha, 1992; Detrick et al., 1987). We cannot however confirm that all of the OAMLs events we have identified have reversed polarity; in many cases, steeply dipping diffractions or multiples prevent confident assessment of the OAML polarity (Figure S4C). However, this does not invalidate our interpretation because apparently normal or ambiguous waveform polarity of partially molten sills is common in MOR seismic reflection studies (e.g., Arnulf et al., 2014; Collier & Sinha, 1992; Detrick et al., 1987).

Under the southern flank of the GSC, the presence of OAMLs could be related to increased magmatism associated to the WDL and Central lineament (Mittelstaedt et al., 2012; Sinton et al., 2003), which are accompanied by a southward shift of the axial mantle LVZ (Figure 2A). However OAMLs are also observed beneath the northern ridge flank (Figure 3A), and in both cases, these events tend to be located near the edges of the axial crustal LVZ. This situation is similar to the OAMLs observed off the EPR (Canales et al., 2012) and suggests that these features form in a region of strong thermal and rheological gradients (e.g., Menand, 2011) where crustal cooling may favor the solidification of melt near the edges of the axial crustal melt reservoir. Alternatively, off-axis melt emplacement may be a response to bending stresses that promote vertical melt extraction from a sublithospheric melt channel, although this mechanism is more efficient at distances of ~10–20 km from the ridge axis (Sohn & Sims, 2005).

4.4. Moho

We observe reflections beneath the southern ridge flank along cross-axis profile S2A at 6.7-km depth bsf that we interpret as Moho (Figure 2). In unmigrated gathers, the Moho is observed as a nearly flat (small

moveout) event at ~2.3 s bsf from near to far offsets (Figure S4D), a character typical of Moho events in the vicinity of MORs (e.g., Aghaei et al., 2014; Canales et al., 2009; Nedimović et al., 2005). We observe that the polarity of the Moho matches that of the seafloor reflection (Figure S6). Our crustal thickness measurement is ~750 m thinner than the 7.45 ± 0.25 km inferred from wide-angle seismic data ~25–30 km to the north of the ridge axis in this region (Canales et al., 2002). This discrepancy could be due to north-south variation in crustal thickness in the study area and/or due to the different ways that near-vertical and wide-angle seismic data sample a Moho transition zone of finite thickness (e.g., Mutter & Carton, 2013). An important observation is that Moho reflection amplitude diminishes relatively abruptly toward the axial zone, eventually disappearing over the tomographically inferred mantle LVZ within ~3 km of the ridge axis (Figure 2). This is most likely due to a combination of attenuation of seismic energy traveling through the axial crustal LVZ (Wilcock et al., 1995) and that Moho across the mantle LVZ may not correspond to a large impedance contrast due to elevated temperatures and presence of melt (13% melt; Canales et al., 2014). The seismic energy gets significantly attenuated within the axial magma chamber, so a sharp contrast in physical properties is required to be present at the Moho for it to be clearly imaged in a seismic section (Singh et al., 2006; Wilcock et al., 1995).

A short, high amplitude reflection is observed along profile AA4 at its intersection with profile S2B at Moho depths (Figures 2A and 3B). Although this event could be interpreted as evidence for on-axis Moho or a partially molten sill at or just above the Moho, we prefer to interpret this event as an artifact due to out-of-line side echoes because it is absent on the perpendicular profile S2B and it is accompanied by migration "smiles" characteristic of overmigration, suggesting that its origin is somewhere shallower in the system where velocities are lower.

5. Conclusions

In this study, we have performed PSDM of 2-D MCS reflection data to provide new constraints on the structure of the axial magma system of the western GSC, using background *P* wave velocities previously derived from the 3-D seismic refraction tomography. In our new PSDM images, we observe segmentation of the shallow AML. A prominent AML gap underlays a mature and waning hydrothermal field, evidencing magmatic-hydrothermal interactions. Here high-temperature hydrothermal activity is restricted to sites over the edges of the AML gap, suggesting that fluids tap heat from the neighboring AML segments to the west and east of the gap. We also observe SAMLs intruding and accreting the lower crust. Some of these SAMLs are present even where the AML is absent, suggesting that melt transfer from the lower crustal reservoir to the shallow AML is episodic. We find evidence for OAMLs forming at the edges of the tomographically imaged axial LVZ, which suggests that OAMLs form preferentially in a region with large rheological contrasts. Moho reflections are observed at distances larger than ~3 km from the axis but disappear abruptly across the axial LVZ where elevated temperatures and presence of partial melt increase the attenuation and diminish the impedance contrast across the crust/mantle boundary.

From the above observations, we conclude that the similarities of the GSC magmatic system (i.e., presence of off-axis and lower crustal sills) with that of the EPR support the idea that these are features found along the global MOR system where seafloor spreading is dominated by magmatic accretion.

Acknowledgments
Seismic data used in this study are available at https://doi.org/10.1594/IEDA/314480 (Detrick & Sinton, 2014). Data processing was conducted with Emerson-Paradigm Software package *Echos* licensed to Woods Hole Oceanographic Institution under Paradigm Academic Software Program. B. B. is funded by the Graduate School of the National Oceanography Centre Southampton UK. We thank two anonymous reviewers for their constructive and insightful comments that helped us in improving the manuscript and A. S. Soule for fruitful discussions.

References

Aghaei, O., Nedimovič, M. R., Carton, H., Carbotte, S. M., Canales, J. P., & Mutter, J. C. (2014). Crustal thickness and Moho character of the fast-spreading East Pacific Rise from 9°42′N to 9°57′N from poststack-migrated 3-D MCS data. *Geochemistry, Geophysics, Geosystems*, *15*, 634–657. https://doi.org/10.1002/2013GC005069

Aghaei, O., Nedimović, M. R., Marjanović, M., Carbotte, S. M., Canales, J. P., Carton, H., & Nikić, N. (2017). Constraints on melt content of off-axis magma lenses at the East Pacific Rise from analysis of 3-D seismic amplitude variation with angle of incidence. *Journal of Geophysical Research: Solid Earth*, *122*, 4123–4142. https://doi.org/10.1002/2016JB013785

Arnulf, A. F., Singh, S. C., & Pye, J. W. (2014). Seismic evidence of a complex multi-lens melt reservoir beneath the 9°N overlapping spreading center at the East Pacific Rise. *Geophysical Research Letters*, *41*, 6109–6115. https://doi.org/10.1002/2014GL060859

Baker, E. T., Haymon, R. M., Resing, J. A., White, S. M., Walker, S. L., Macdonald, K. C., & Nakamura, K. I. (2008). High-resolution surveys along the hot spot-affected Galápagos Spreading Center: 1. Distribution of hydrothermal activity. *Geochemistry, Geophysics, Geosystems*, *9*, Q09003. https://doi.org/10.1029/2008GC002028

Blacic, T. M., Ito, G., Canales, J. P., Detrick, R. S., & Sinton, J. (2004). Constructing the crust along the Galapagos Spreading Center 91.3°-95.5°W: Correlation of seismic layer 2A with axial magma lens and topographic characteristics. *Journal of Geophysical Research*, *109*, B10310. https://doi.org/10.1029/2004JB003066

Boudier, F., Adolphe, N., & Ildefonse, B. (1996). Magma chambers in the Oman ophiolite: Fed from the top and the bottom. *Earth and Planetary Science Letters*, *144*(1–2), 239–250. https://doi.org/10.1016/0012-821X(96)00167-7

Canales, J., Ito, G., Detrick, R. S., & Sinton, J. (2002). Crustal thickness along the western Galápagos Spreading Center and the compensation of the Galápagos hotspot swell. *Earth and Planetary Science Letters*, *203*(1), 311–327. https://doi.org/10.1016/S0012-821X(02)00843-9

Canales, J. P., Carton, H., Carbotte, S. M., Mutter, J. C., Nedimović, M. R., Xu, M., et al. (2012). Network of off-axis melt bodies at the East Pacific Rise. *Nature Geoscience*, *5*(4), 279–283. https://doi.org/10.1038/ngeo1377

Canales, J. P., Dunn, R. A., Ito, G., Detrick, R. S., & Sallarès, V. (2014). Effect of variations in magma supply on the crustal structure of mid-ocean ridges: Insights from the Western Galápagos Spreading Center. In *The Galapagos: A natural laboratory for the Earth sciences* (pp. 363–391). Washington, DC: American Geophysical Union. https://doi.org/10.1002/9781118852538.ch17

Canales, J. P., Nedimovi, M. R., Kent, G. M., Carbotte, S. M., & Detrick, R. S. (2009). Seismic reflection images of a near-axis melt sill within the lower crust at the Juan de Fuca ridge. *Nature*, *460*(7251), 89–93. https://doi.org/10.1038/nature08095

Carbotte, S. M., Marjanović, M., Carton, H., Mutter, J. C., Canales, J. P., Nedimović, M. R., et al. (2013). Fine-scale segmentation of the crustal magma reservoir beneath the East Pacific Rise. *Nature Geoscience*, *6*(10), 866–870. https://doi.org/10.1038/ngeo1933

Carbotte, S. M., Smith, D. K., Cannat, M., & Klein, E. M. (2016). Tectonic and magmatic segmentation of the global ocean ridge system: A synthesis of observations. *Geological Society, London, Special Publications*, *420*(1), 249–295. https://doi.org/10.1144/SP420.5

Choo, J., Downton, J., & Dewar, J. (2004). LIFT: A new and practical approach to noise and multiple attenuation. *First Break*, *22*(1012), 39–44. https://doi.org/10.3997/1365-2397.2004009

Christie, D. M., Werner, R., Hauff, F., Hoernle, K., & Hanan, B. B. (2005). Morphological and geochemical variations along the eastern Galápagos Spreading Center. *Geochemistry, Geophysics, Geosystems*, *6*, Q01006. https://doi.org/10.1029/2004GC000714

Collier, J. S., & Sinha, M. C. (1992). Seismic mapping of a magma chamber beneath the Valu Fa Ridge, Lau Basin. *Journal of Geophysical Research*, *97*(B10), 14031. https://doi.org/10.1029/91jb02751

Detrick, R. S., Buhl, P., Vera, E., Mutter, J., Orcutt, J., Madsen, J., & Brocher, T. (1987). Multi-channel seismic imaging of a crustal magma chamber along the East Pacific Rise. *Nature*, *326*(6108), 35–41. https://doi.org/10.1038/326035a0

Detrick, R. S., & Sinton, J. M. (2014). Raw multi-channel seismic shot data from the Galapagos Spreading Center acquired during R/V Maurice Ewing expedition EW0004 (2000), Interdisciplinary Earth Data Alliance (IEDA). https://doi.org/10.1594/IEDA/314480

Detrick, R. S., Sinton, J. M., Ito, G., Canales, J. P., Behn, M., Blacic, T., et al. (2002). Correlated geophysical, geochemical, and volcanological manifestations of plume-ridge interaction along the Galápagos Spreading Center. *Geochemistry, Geophysics, Geosystems*, *3*(10), 8501. https://doi.org/10.1029/2002GC000350

Dunn, R. A., Toomey, D. R., & Solomon, S. C. (2000). Three-dimensional seismic structure and physical properties of the crust and shallow mantle beneath the East Pacific Rise at 9°30′N. *Journal of Geophysical Research*, *105*(B10), 23,537–23,555. https://doi.org/10.1029/2000JB900210

Fontaine, F. J., Olive, J. A., Cannat, M., Escartin, J., & Perol, T. (2011). Hydrothermally-induced melt lens cooling and segmentation along the axis of fast-and intermediate-spreading centers. *Geophysical Research Letters*, *38*, L14307. https://doi.org/10.1029/2011GL047798

Han, S., Carbotte, S. M., Canales, J. P., Carton, H., Nedimović, M. R., Gibson, J., & Horning, G. (2016). Seismic reflection imaging of the Juan de Fuca plate from ridge to trench: New constraints on the distribution of faulting and evolution of the crust prior to subduction. *Journal of Geophysical Research: Solid Earth*, *121*, 1849–1872. https://doi.org/10.1002/2015JB012416

Han, S., Carbotte, S. M., Carton, H., Mutter, J. C., Aghaei, O., Nedimović, M. R., & Canales, J. P. (2014). Architecture of on- and off-axis magma bodies at EPR 9°37–40′N and implications for oceanic crustal accretion. *Earth and Planetary Science Letters*, *390*, 31–44. https://doi.org/10.1016/j.epsl.2013.12.040

Harding, A. J., Kent, G. M., & Orcutt, J. A. (1993). A multichannel seismic investigation of upper crustal structure at 9°N on the East Pacific Rise: Implications for crustal accretion. *Journal of Geophysical Research*, *98*(B8), 13,925–13,944. https://doi.org/10.1029/93JB00886

Harpp, K., & Geist, D. (2002). Wolf-Darwin lineament and plume-ridge interaction in northern Galápagos. *Geochemistry, Geophysics, Geosystems*, *3*(11), 8504. https://doi.org/10.1029/2002GC000370

Haymon, R. M., White, S. M., Baker, E. T., Anderson, P. G., Macdonald, K. C., & Resing, J. A. (2008). High-resolution surveys along the hot spot-affected Galápagos Spreading Center: 3. Black smoker discoveries and the implications for geological controls on hydrothermal activity. *Geochemistry, Geophysics, Geosystems*, *9*, Q12006. https://doi.org/10.1029/2008GC002114

Henstock, T. J., Woods, A. W., & White, R. S. (1993). The accretion of oceanic crust by episodic sill intrusion. *Journal of Geophysical Research*, *98*(B3), 4143–4161. https://doi.org/10.1029/92JB02661

Hey, R., & Vogt, P. (1977). Spreading center jumps and sub-axial asthenosphere flow near the Galapagos hotspot. *Tectonophysics*, *37*(1–3), 41–52. https://doi.org/10.1016/0040-1951(77)90038-5

Ito, G., & Lin, J. (1995). Mantle temperature anomalies along the present and paleoxes of the Galapagos Spreading Center as inferred from gravity analyses. *Journal Geophysical Research: Solid Earth*, *100*(B3), 3733–3745. https://doi.org/10.1029/94JB02594

Kelemen, P. B., & Aharonov, E. (1998). Periodic formation of magma fractures and generation of layered gabbros in the lower crust beneath oceanic spreading ridges. In W. R. Buck, et al. (Eds.), *Faulting and Magmatism at Mid-Ocean Ridges*, *Geophysical Monograph Series* (Vol. 106, pp. 267–289). Washington, DC: American Geophysical Union. https://doi.org/10.1029/GM106p0267

Kelemen, P. B., Koga, K., & Shimizu, N. (1997). Geochemistry of gabbro sills in the crust-mantle transition zone of the Oman ophiolite: Implications of the origin of the oceanic lower crust. *Earth and Planetary Science Letters*, *8*(1), 186–188. https://doi.org/10.1093/ilj/8.1.186

Kent, G. M., Harding, A. J., & Orcutt, J. A. (1993). Distribution of magma beneath the East Pacific Rise between the Clipperton Transform and the 9°17′N Deval from forward modeling of common depth point data. *Journal of Geophysical Research*, *98*(B8), 13,945–13,969. https://doi.org/10.1029/93JB00705

Korenaga, J., & Kelemen, P. (1998). Melt migration through the oceanic lower crust: A constraint from melt percolation modeling with finite solid diffusion. *Earth and Planetary Science Letters*, *156*(1-2), 1–2), 1–11. https://doi.org/10.1016/s0012-821x(98)00004-1

Lissenberg, C. J., MacLeod, C. J., Howard, K. A., & Godard, M. (2013). Pervasive reactive melt migration through fast-spreading lower oceanic crust (Hess Deep, equatorial Pacific Ocean). *Earth and Planetary Science Letters*, *361*, 436–447. https://doi.org/10.1016/j.epsl.2012.11.012

Maclennan, J., Hulme, T., & Singh, S. C. (2004). Thermal models of oceanic crustal accretion: Linking geophysical, geological and petrological observations. *Geochemistry, Geophysics, Geosystems*, *5*, Q02F25. https://doi.org/10.1029/2003GC000605

Marjanović, M., Carbotte, S. M., Carton, H., Nedimović, M. R., Mutter, J. C., & Canales, J. P. (2014). A multi-sill magma plumbing system beneath the axis of the East Pacific Rise. *Nature Geoscience*, *7*(11), 825–829. https://doi.org/10.1038/ngeo2272

Marjanović, M., Carbotte, S. M., Carton, H. D., Nedimović, M. R., Canales, J. P., & Mutter, J. C. (2018). Crustal magmatic system beneath the East Pacific Rise (8°20′ to 10°10′ N): Implications for tectono-magmatic segmentation and crustal melt transport at fast-spreading ridges. *Geochemistry, Geophysics, Geosystems*, *19*(11), 4584–4611. https://doi.org/10.1029/2018GC007590

Menand, T. (2011). Physical controls and depth of emplacement of igneous bodies: A review. *Tectonophysics*, *500*(1–4), 11–19. https://doi.org/10.1016/j.tecto.2009.10.016

Mittelstaedt, E., Soule, S., Harpp, K., Fornari, D., McKee, C., Tivey, M., et al. (2012). Multiple expressions of plume-ridge interaction in the Galápagos: Volcanic lineaments and ridge jumps. *Geochemistry, Geophysics, Geosystems*, *13*, Q05018. https://doi.org/10.1029/2012GC004093

Mutter, J. C., Carbotte, S., Nedimovic, M., Canales, J. P., & Carton, H. (2009). Seismic imaging in three dimensions on the East Pacific Rise. *Eos, Transactions American Geophysical Union*, *90*(42), 374–375. https://doi.org/10.1029/2009EO420002

Mutter, J. C., & Carton, H. D. (2013). The mohorovicic discontinuity in ocean basins: Some observations from seismic data. *Tectonophysics*, *609*, 314–330. https://doi.org/10.1016/j.tecto.2013.02.018

Nedimovič, M. R., Carbotte, S. M., Harding, A. J., Detrick, R. S., Canales, J. P., Diebold, J. B., et al. (2005). Frozen magma lenses below the oceanic crust. *Nature*, *436*(7054), 1149–1152. https://doi.org/10.1038/nature03944

Quick, J. E., & Denlinger, R. P. (1993). Ductile deformation and the origin of layered gabbro in ophiolites. *Journal of Geophysical Research*, *98*(B8), 14,015–14,027. https://doi.org/10.1029/93JB00698

Rubin, K. H., & Sinton, J. M. (2007). Inferences on mid-ocean ridge thermal and magmatic structure from MORB compositions. *Earth and Planetary Science Letters*, *260*(1–2), 257–276. https://doi.org/10.1016/j.epsl.2007.05.035

Singh, S. C., Harding, A. J., Kent, G. M., Sinha, M. C., Combier, V., Bazin, S., et al. (2006). Seismic reflection images of the Moho underlying melt sills at the East Pacific Rise. *Nature*, *442*(7100), 287–290. https://doi.org/10.1038/nature04939

Sinton, J., Detrick, R., Canales, J. P., Ito, G., & Behn, M. (2003). Morphology and segmentation of the western Galápagos spreading center, 90.5°-98°W: Plume-ridge interaction at an intermediate spreading ridge. *Geochemistry, Geophysics, Geosystems*, *4*(12), 8515. https://doi.org/10.1029/2003GC000609

Sohn, R. A., & Sims, K. W. W. (2005). Bending as a mechanism for triggering off-axis volcanism on the East Pacific Rise. *Geology*, *33*(2), 93–96. https://doi.org/10.1130/G21116.1

Soubaras, R. (1996). Explicit 3-D migration using equiripple polynomial expansion and Laplacian synthesis. *Geophysics*, *61*(5), 1386–1393. https://doi.org/10.1190/1.1444062

Wilcock, W. S. D., Solomon, S. C., Purdy, G. M., & Toomey, D. R. (1995). Seismic attenuation structure of the East Pacific Rise near 9°30′N. *Journal of Geophysical Research*, *100*(B12), 24,147–24,165. https://doi.org/10.1029/95JB02280

Wilson, D. S., & Hey, R. N. (1995). History of rift propagation and magnetization intensity for the Cocos-Nazca spreading center. *Journal of Geophysical Research*, *100*(B6), 10,041–10,056. https://doi.org/10.1029/95JB00762